Radiation-induced segregation in a ceramic

Xing Wang[1,*,§], Hongliang Zhang[2,§], Tomonori Baba[1], Hao Jiang[2], Cheng Liu[1], Yingxin Guan[3], Omar Elleuch[3], Thomas Kuech[3], Dane Morgan[1,2], Juan-Carlos Idrobo[4], Paul M. Voyles[2], Izabela Szlufarska[1,2,*]

[1] Department of Engineering Physics and Nuclear Engineering, University of Wisconsin-Madison, WI, USA, 53706
[2] Department of Materials Science and Engineering, University of Wisconsin-Madison, WI, USA, 53706
[3] Department of Chemical and Biological Engineering, University of Wisconsin-Madison, WI, USA, 53706
[4] Center for Nanophase Materials Sciences, Oak Ridge National Laboratory, Oak Ridge, TN, USA, 37831

* Corresponding authors
[§] Co-first authors

Abstract

We discover that radiation can induce significant segregation of one of the constituent elements to grain boundaries (GBs) in a ceramic, despite the fact that the ceramic forms a line-compound and therefore has a strong thermodynamic driving force to resist off-stoichiometry. Specifically, irradiation of silicon carbide (SiC) at 300°C leads to carbon enrichment near GBs whereas the enrichment diminishes for irradiation at 600°C. The temperature dependence of this radiation-induced segregation (RIS) is different from that shown in metallic systems. Using an *ab initio* informed rate-theory model, we demonstrate that the different RIS temperature dependence in SiC is introduced by the unique defect energy landscapes present in the covalent system. In addition, we discover that GBs in unirradiated SiC grown by chemical vapor deposition are intrinsically carbon-depleted. The inherent GB chemistry and its evolution under radiation are both critical for understanding the many properties of ceramics that depend on GBs.

Properties of polycrystalline materials are often controlled by their grain boundaries (GBs) [1], since GBs can act as obstacles for dislocation motions [2], active sites for corrosion reactions [3], sinks for point defects [4], and diffusion channels for solute atoms [5]. Therefore, changes in GBs' atomic structure and chemical composition can often significantly modify the materials' mechanical strength, corrosion resistance, radiation tolerance, and imperviousness to radioactive fission products.

Radiation-induced segregation (RIS) is one of the most dramatic changes that can take place in GBs under irradiation or ion implantation. RIS has been observed in many metallic alloys [6–9]. Under irradiation, a large number of Frenkel pairs are generated by the bombardment of incident particles like neutrons and ions. These defects can either recombine with each other or migrate to defect sinks, such as surfaces and GBs [10]. In multi-component alloys, because of the different diffusivities of elements mediated by these defects, the fluxes of the elemental species to GBs may not match the stoichiometry of the host. As a result, there will be a build-up or depletion of certain elements in the vicinity of GBs [8,11,12]. Up to this point RIS has not been reported in ceramics. In particular, many ceramics form line compounds (such as SiC [13]), and it is an open question whether a material that forms a line-compound can exhibit RIS or whether the thermodynamic driving force for stoichiometry is strong enough to suppress any significant segregation of constituent elements. If RIS does occur in such line compounds, it is not clear if it would involve formation of new phases or off-stoichiometric phase compositions outside those seen in the bulk phase diagram.

Using electron energy loss spectroscopy (EELS) in an aberration-corrected scanning transmission electron microscope (STEM), we discovered the existence of RIS of a primary component in a ceramic, i.e., carbon in SiC. We chose SiC as a representative covalent ceramic, but it is also a promising structural material for advanced nuclear reactors and microelectromechanical systems operating in harsh conditions [14,15]. Interestingly, we found that segregation in SiC occurred at a much lower irradiation temperature than typical RIS in metals. GBs became carbon-enriched for irradiation at 300°C, which was 0.18 of the SiC melting temperature (T_m), and the segregation was suppressed at 600°C ($0.28T_m$). In contrast, RIS are most significant between $0.3T_m$ and $0.5T_m$ in metallic alloys [10]. The much lower temperature for RIS in SiC suggests that the understanding of RIS in metals

may not be simply transferred to ceramics. Unlike metal alloys, ceramics have much more complex energy landscapes for defect reactions and multiple sublattices on which defects can migrate [16]. Here, we developed an *ab initio*-informed rate theory model that reproduced and explained the trend of RIS with temperature. Our calculations reveal that the off-stoichiometric defect fluxes to GBs are controlled by both the defect migration energy barriers and the recombination barriers, leading to the unique temperature dependence of RIS in SiC.

Intrinsic carbon-depletion of GBs in SiC

As a reference for our RIS measurement, it is first necessary to quantify the GB composition in non-irradiated SiC. Here, we use STEM imaging to locate the GB positions and EELS spectrum imaging to quantify the local carbon concentration. Fig. 1a is a typical STEM high-angle annular dark field (HAADF) image of GBs in pristine SiC. The image is acquired using the Nion UltraSTEM 100™ operating at 60 kV [17]. Twin boundaries, coincidence site lattice grain boundaries (CSLGBs) and general high-angle GBs (HAGBs) can all be identified in the image. We focus on HAGBs in this study because HAGBs are the most common type of GBs in 3C-SiC fabricated by chemical vapor deposition (CVD), accounting for more than half of the total GBs [18]. Fig. 1b shows a closer view of the HAGB. Since HAGBs usually consist of both tilt and twist misorientations, atomic resolution can only be achieved on one side of the boundary. In Fig. 1b, the boundary width is less than 2 nm, indicating the GB is almost parallel to the incident electron beam. Tilting the sample properly to this edge-on orientation is critical to the local composition measurement as a function of distance to GB. A spectrum image is acquired in the rectangular region across the GB (i.e., the white box), and the average carbon concentration at certain distance to GB is calculated based on EELS signals summed inside the narrow red box. The width of the red box and the step size for moving the red box are both around or less than 5 Å. For simplicity, we will refer to HAGBs as GBs in the remainder of the text, unless specified otherwise.

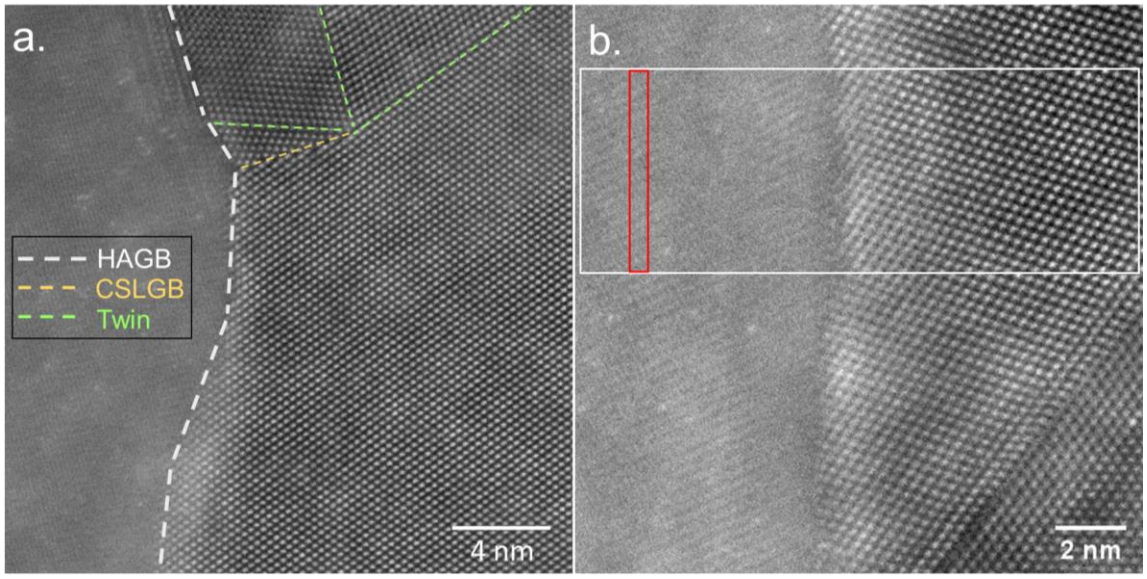

Figure 1 (a) STEM-HAADF image showing different types of GBs in SiC. (b) The white box highlights the region where the EELS spectrum image is obtained while the narrow red box highlights the region where the EELS spectrum is processed to obtain the averaged local carbon concentration at a certain distance from the GB. More details related to the EELS experiment can be found in Methods.

To ensure that the results are reproducible, similar STEM-EELS measurements were performed on seven GBs found in pristine SiC thin foils prepared using either focused ion beam (FIB) milling or mechanical polishing. For each GB, more than three spectrum images were acquired, and the corresponding carbon concentration profiles were measured. Individual measurements of the seven GBs are summarized in supplementary information (SI) note 1. Based on multiple measurements from different samples, the averaged carbon concentrations as a function of distance to GB are calculated and plotted in Fig. 2a. For comparison, similar EELS measurements are also performed in the grain interiors and the carbon concentration profile is shown in Fig. 2b. In a highly pure SiC, carbon concentration is expected to be 50 at. %, which is exactly the case shown in the grain interiors. However, as shown in Fig. 2a, carbon concentration is obviously reduced in the vicinity of the GBs (within a ~2 nm thick region) with a minimum value of 45.8±0.4 at. % right at the boundary. In addition, multiple measurements from different GBs suggest that the carbon depletion is a general property of HAGBs and independent of the boundary misorientation angles.

Table 1 summarizes carbon concentrations at the boundary in different GBs, as well as the corresponding Miller index and the misorientation angle of each GB determined using transmission electron backscatter diffraction (tEBSD). Although the misorientation angles vary from 29º to 59º in different GBs, similar intrinsic carbon depletion at about 45.8 at. % are observed at all of these GBs.

It is worth noting that the carbon concentrations shown in Fig. 2a are indeed relative concentrations, which raises the question whether the valley in the concentration profile is introduced by carbon depletion or silicon enrichment. To answer this question, we also calculate the peak counts ratio, $\phi(x)$, for both silicon and carbon. Here x is the distance to GB and $\phi(x)$ is defined as the ratio of EELS peak counts of one element at x to the average peak counts of the same element in the grain interior. Since EELS peak count is proportional to the atomic density of the element in the material, $\phi(x)$ represents the percentage change of the element densities near GBs referenced to the grain interior. In Fig. 2c, $\phi(x)$ of both silicon and carbon drop below 1 near the GB, indicating the atomic densities for both elements get lower at the GB, which is reasonable because GBs are structurally more disordered than the crystalline grain. However, $\phi(0)$ for carbon is about 83% whereas $\phi(0)$ for silicon is about 96%, demonstrating the lower relative carbon concentration is due to carbon depletion, rather than silicon enrichment

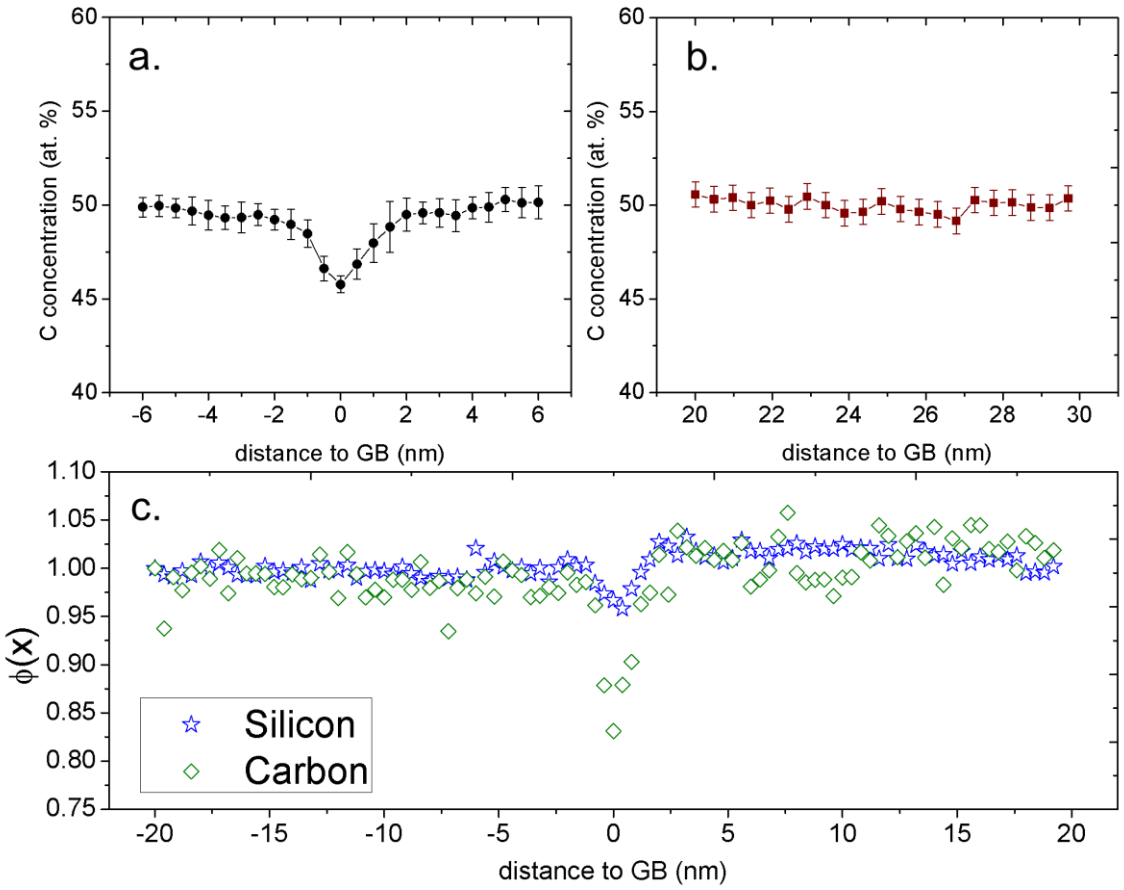

Figure 2 (a) Average relative carbon concentration near GBs. The concentration profile is obtained by averaging multiple EELS measurements of seven GBs, and the standard deviations of multiple measurements from seven GBs are taken as the uncertainty. (b) Carbon concentration in grain interior from one EELS measurement. The standard deviation of the carbon concentration values measured in the grain interiors is taken as the uncertainty of the carbon concentration measurement. (c) Peak counts ratio $\phi(x)$ for silicon (blue stars) and carbon (green diamonds) near a GB based on one characteristic EELS measurement near a GB.

Table 1 Summary of individual EELS measurement results of non-irradiated GBs

GB No.	C conc. (at. %)	Fab.	T_{anneal}	mis. angle	Miller index
1	45.2	FIB	300ºC	59º	(3 -1 1) // (-1 -14 -15)
2	46.3	FIB	300ºC	45º	(-2 30 -31) // (-3 9 -10)
3	46.4	FIB	500ºC	59º	(-13 -1 -7) // (-8 -6 -3)
4	45.6	FIB	600ºC	29º	(6 -2 5) // (-6 5 -7)
5	45.3	Polish	600ºC	-	-
6	45.9	Polish	-	-	-
7	45.7	Polish	-	-	-

Note: GBs with an annealing temperature (T_{anneal}) means the GB is obtained from an irradiated bulk sample but the GB locates deeper than the range of the ion radiation damage, which is 2.2 μm below the surface for 3.15 MeV carbon ions into SiC. Therefore, these GBs receive zero radiation damage, and T_{anneal} is the irradiation temperature. The misorientation angle and Miller index of GB planes are determined by comparing tEBSD mapping and correlated transmission electron microscope (TEM) images. Fabrication (Fab.) is the method used for preparing the thin foil for STEM-EELS measurements, either FIB or mechanical polishing. Correlative tEBSD and TEM comparison was not performed on thin foils prepared by mechanical polishing due to technical difficulties, so the GB misorientation angles and Miller indexes are not provided for these GBs. More details about thin foil preparation and the correlative tEBSD and TEM analysis are provided in Methods.

To the best of our knowledge, the intrinsic carbon depletion near GBs in CVD 3C-SiC has not been reported before. It is not clear whether the carbon-depleted GB is only a metastable phase generated during the CVD process, or it has a lower energy than a stoichiometric GB. However, it is clear that this is a common feature of the CVD grown SiC samples. Since CVD is a widely-adopted technique for SiC fabrication [19,20], it is meaningful to explore the origin of the carbon depletion and its potential effects on various

GB-controlled materials properties, such as corrosion resistance in future studies. We want to emphasize that the carbon concentration of the pristine GBs should not affect the defect migration and element segregation to defect sinks. Previous experiments have demonstrated that GBs in CVD 3C-SiC, which are probably intrinsically carbon-depleted, act as efficient defect sinks [21,22]. Meanwhile, simulation studies have confirmed that stoichiometric GBs are defect sinks as well and that excess carbon at GBs can be easily accommodated as antisite defects [23,24].

Radiation-induced carbon enrichment at GBs

Bulk CVD 3C-SiC samples were irradiated by 3.15 MeV carbon ion to a total fluence of 1.50×10^{17} ions/cm^2, which generated an average damage of 1 displacement per atom (dpa) within 1 μm of the sample surface based on Stopping and Range of Ions in Matter (SRIM) package calculations [25,26]. One batch of the samples was irradiated at 300°C and the other batch was irradiated at 600°C. Following the same procedures for thin foils preparation and EELS measurement, we characterized four GBs irradiated at 300°C and two GBs irradiated at 600°C. Fig. 3 shows the average carbon concentration profiles near GBs calculated based on multiple measurements from different GBs. Characterization results of each irradiated GB are summarized in SI note 2. An obvious GB composition evolution at different irradiation temperatures can be found by comparing Figs. 3a, 3b, and 2a. At 300°C, the intrinsic carbon depletion almost disappears, and the carbon concentrations increase to around 48.9±0.6 at. % at the GBs (Fig. 3a). However, the carbon concentration near GBs drops again at 600°C to a minimum value around 47.2±0.7% (Fig. 3b). Similar peak counts ratios $\phi(x)$ near these irradiated GBs are also calculated. As shown in Fig. 3c, unlike the non-irradiated GBs in Fig. 2c, $\phi(x)$ of both carbon and silicon exhibit a plateau near GBs irradiated at 300°C. Therefore, the radiation-induced carbon enrichment is mostly introduced by the carbon segregation to GBs, rather than the silicon diffusion away from the GBs. At 600°C, $\phi(x)$ for carbon are obviously lower than silicon $\phi(x)$ indicating the segregation behaviors of carbon to GB is suppressed as the irradiation temperature increases.

Table 2 summarizes the GB carbon concentrations and the corresponding boundary parameters determined by tEBSD for each irradiated GBs. The misorientation angles of these irradiated GBs are quite close to angles of the non-irradiated GBs in Table 1, so it is reasonable to assume the irradiated GBs had a similar intrinsic carbon-depletion before the irradiation. Despite the varying boundary misorientation angles, similar RIS is observed in all the different GBs, suggesting the segregation phenomenon is not associated with certain types of HAGBs.

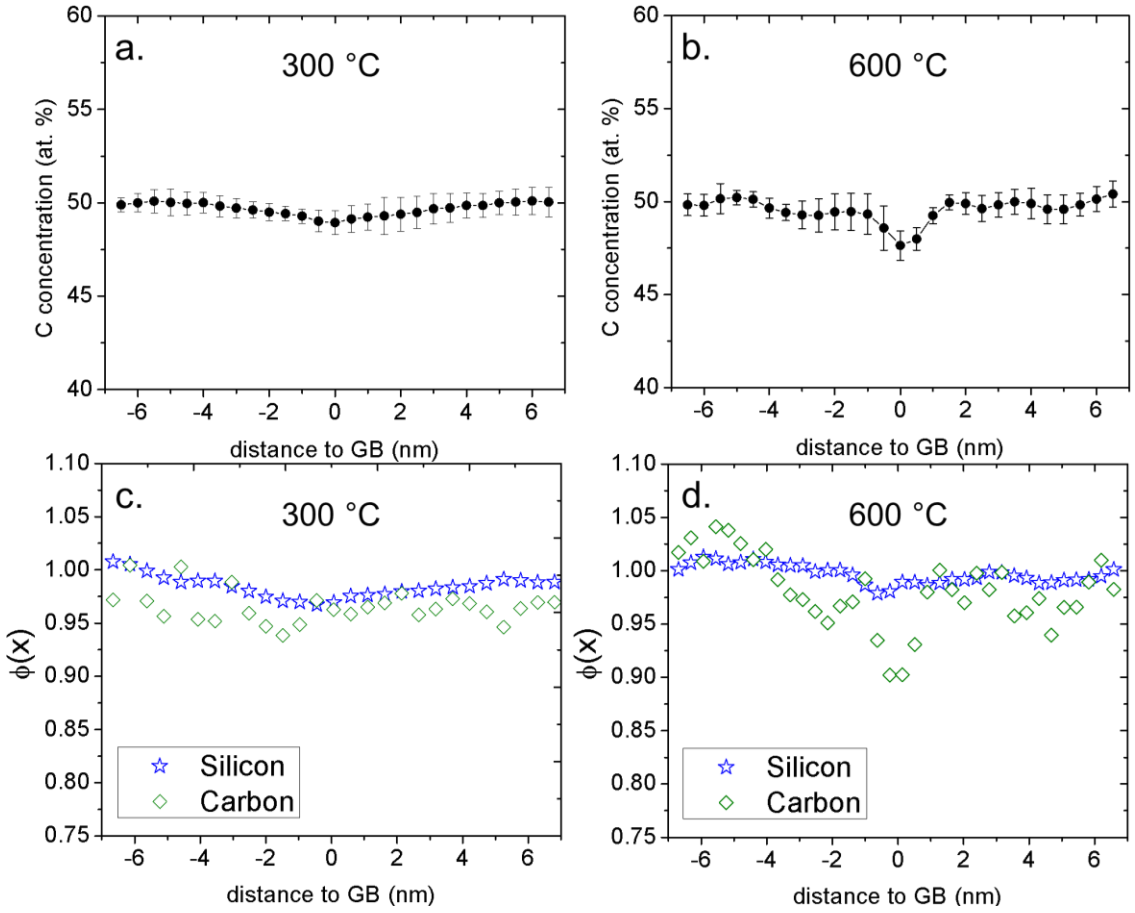

Figure 3 Average carbon concentration profile measured near GBs in irradiated SiC at (a) 300°C and (b) 600°C. Typical peak count ratios near GBs irradiated at (c) 300°C and (d) 600°C. In (a) and (b), standard deviations of multiple measurements from different GBs are shown as uncertainties of the carbon concentration values.

Table 2 Summary of results of individual EELS measurement of irradiated GBs

GB No.	C conc. (at. %)	Fab.	T_{irr}	mis. angle	Miller index
1	48.9	FIB	300ºC	21º	(-25 -3 -1) // (18 1 -6)
2	49.0	FIB	300ºC	51º	(-3 -8 -7) // (-2 -48 3)
3	48.9	Polish	300ºC	-	-
4	49.1	Polish	300ºC	-	-
5	46.9	FIB	600ºC	59º	(4 -14 1) // (-3 -22 16)
6	47.4	FIB	600ºC	35º	(-3 -6 -4) // (7 1 10)

Note: T_{irr} is the irradiation temperature. For other columns please refer to note of Table 1.

We exclude the possibility that the observed segregation is introduced by concentrating the implanted carbon ions near GBs or damaging the materials by the electron beam during STEM analysis. First of all, the amount of implanted carbon is negligible when compared to the atom number in the sample. As detailed in SI note 3, even if we assume all the implanted carbon ions are concentrated within 2 nm of GBs as an upper bound estimation, the relative carbon concentration at GBs would be increased only from 45.8 at. % to 47.3 at. %, which is still smaller than the carbon enrichment shown in 300ºC experiment. In addition, if diffusion of implanted C was responsible for the observed carbon enrichment, enrichment would be also evident in GBs that are about 4 μm below the surface of irradiated bulk samples (i.e., GBs 1-5 in Table 1). These GBs are deeper than the maximum depth of the implanted carbon (2.2 μm), so they receive zero radiation, but the implanted carbon could still diffuse to and concentrate near these GBs during the irradiation experiment. As shown in Table 1, such GBs exhibit similar intrinsic carbon depletion, demonstrating that the GB compositions are not influenced by the exotic implanted carbon. With respect to the possible electron beam damage in materials, according to the elastic scattering theory [27], the maximum recoil energy transferred (R_{max}) from an electron to an atom is

$$R_{max} = \frac{2E(E+2m_0c^2)}{Mc^2}. \quad (1)$$

Here, E is the incident electron beam energy, m_0 is the static electron mass, M is the atom mass and c is speed of light. For 60 keV electron used in this study, R_{max} is 4.9 eV for Si and is 11.6 eV for C. Both values are much lower than the corresponding displacement threshold energy (32 eV for Si and 19 eV for C in SiC [28]), so the 60 keV electron beam is not able to generate collision damage or local composition change in SiC. From the above analyses, it is clear that radiation leads to the enrichment of carbon at 300°C and this radiation effect is suppressed during 600°C irradiation. To further validate the observed RIS phenomenon, we have performed additional irradiation experiments using 4.5 MeV Si ion on bicrystal SiC samples and the samples were subsequently analyzed using EELS. Very similar intrinsic carbon depletion near pristine GBs and carbon enrichment near irradiated GBs at 300°C have been found. Detailed results from the bicrystal samples irradiated by Si ions are discussed in SI note 4.

Temperature dependence of RIS in SiC

The melting temperature of SiC is 2830°C [29], which means that RIS in SiC occurs at $0.18T_m$ (300°C). This relative temperature is lower than the reported RIS temperatures in common metallic alloys (between $0.3T_m$ and $0.5T_m$) [10]. The temperature dependence of RIS in metals has been successfully explained based on vacancy kinetics at different irradiation temperatures (T_{irr}) since diffusion in those metals has been reported to be vacancy mediated. [30] Specifically, when $T_{irr} < 0.3T_m$, the vacancy mobility is low, so most vacancies would recombine with nearby interstitials generated by irradiation rather than enabling transport of species to GBs. When $T_{irr} > 0.5T_m$, thermal vacancy concentrations increase substantially, again promoting the Frenkel pair recombination in grain interiors rather than chemical diffusion to GBs. In addition, at high temperature the difference in partial diffusivities between alloy elements decreases, and therefore the off-stochiometric defect flux to sinks (such as GBs) is reduced. Only at the intermediate temperature there will be enough mobile vacancies that diffuse to GBs at different rates to generate observable segregation. Unlike metallic alloys, two notable features of defect energetics in SiC lead to the different RIS temperature dependence in the covalent system. First, the

vacancy mobility is extremely low and a large gap of mobilities exists between interstitials and vacancies in SiC. Based on density functional theory (DFT) calculations [31], the vacancy migration barrier is 2.4 eV for carbon and 3.6 eV for silicon, which make vacancies nearly immobile in the investigated temperature range (up to 600°C or even higher). In contrast, interstitials in SiC have similar mobilities to interstitials in metals [31]. Therefore, in SiC it is the interstitials that play the dominant role in the RIS process. Second, DFT calculations have shown that there is a relatively high energy barrier (0.91 eV) for recombination of carbon Frenkel pairs, but such barrier is negligible (0.03 eV) for silicon [16]. The distinct defect energetics for different sublattices selectively suppresses recombination of carbon interstitials with vacancies at lower temperature, and the excess carbon interstitials will segregate to defect sinks like GBs.

To quantify the effects of defect energetics on RIS-temperature dependence in SiC, we developed a rate theory model that connects defect generation, migration, and recombination in both the grain interiors and at the GBs. Specifically, the defect kinetic processes on the carbon and silicon sublattices are calculated by the following equations

$$\frac{\partial C_i(x,t)}{\partial t} = \frac{F_i(t)}{d} + G - Rc_i(x,t)c_v(x,t) + D_i\nabla^2 c_i(x,t) \quad (2)$$

$$\frac{\partial C_v(x,t)}{\partial t} = \frac{F_v(t)}{d} + G - Rc_i(x,t)c_v(x,t) + D_v\nabla^2 c_v(x,t) \quad (3)$$

Here, subscripts *i* and *v* stand for interstitial and vacancy, respectively. $c(x,t)$ is the defect concentration. One the right-hand side of the equations, the first term is the defect flux from the grain interior, which can be regarded as an "external" defect source for the GB. The remaining three terms account for the "internal" point defect generation, recombination, and diffusion along the GB, respectively. Here, d is the width of the GB and $F_{i/v}$ is the interstitials/vacancies flux to GBs, calculated using another model developed for defect evolutions in grain interiors of SiC [32]. R is the coefficient for the Frenkel pair recombination and $D_{i,v}$ are the defect diffusivities along GBs. A cartoon showing all the defect kinetic processes included in this model are presented in Figs. 4a and b. After solving for $c(x,t)$, the carbon concentration at the GB is calculated using Eq. 11 in Methods, where more details related to the model are also provided.

Calculations based on the above model reveal a few important trends in defect fluxes that determine the temperature effects on RIS in SiC. In Fig 4c, we plot the rates at which interstitials arrive at and leave the GB during irradiation. First, the arrival rate of carbon interstitials from the grain interior is much higher than that of silicon interstitial, which provides the driving force for the carbon enrichment near GBs. In addition to the different recombination barriers mentioned earlier, the lower interstitial migration barrier of carbon (0.67 eV) as compared to silicon (0.83 eV) in the grain also contributes to this higher carbon arrival rate [31]. Second, the arrival rate of carbon interstitial decreases as T_{irr} increases. As shown in the cartoon on the left, when T_{irr}=300°C, the recombination of carbon Frenkel pair is mostly suppressed so carbon interstitials can migrate to GBs which act as defect sinks (Fig. 4a). At T_{irr}=600°C, the recombination of carbon Frenkel pair becomes active so the carbon flux to GBs and the segregation decreases (Fig. 4b). Third, the rate at which carbon interstitials migrate along the GBs to other sinks (e.g., surfaces and triple junctions) are much lower than the rate of carbon arrival. This is because the interstitial diffusion along GBs is much slower than interstitial diffusion in grain interiors, which has been discovered in our previous study and provides a necessary condition for RIS [33]. The mechanisms of carbon accommodation at SiC GBs have been studied in detail in Refs.[23,33]. In Fig. 4d, we compare carbon concentrations in the GB from experiment and from simulations. The temperature dependence of RIS is qualitatively reproduced by our model, although the model predicts a larger segregation at 300°C, which will be investigated in future study. It is worth noting that the effects of electronic energy loss from the 3.15 MeV carbon ions are not included in current RIS model. It has been reported in literature that the electronic energy loss form MeV ion irradiation can introduce thermal spikes and promote defect annealing in SiC [34,35], potentially leading to a reduced carbon flux and a lower carbon enrichment near GBs. Effects of the electronic energy loss on the RIS calculations are discussed in SI note 5.

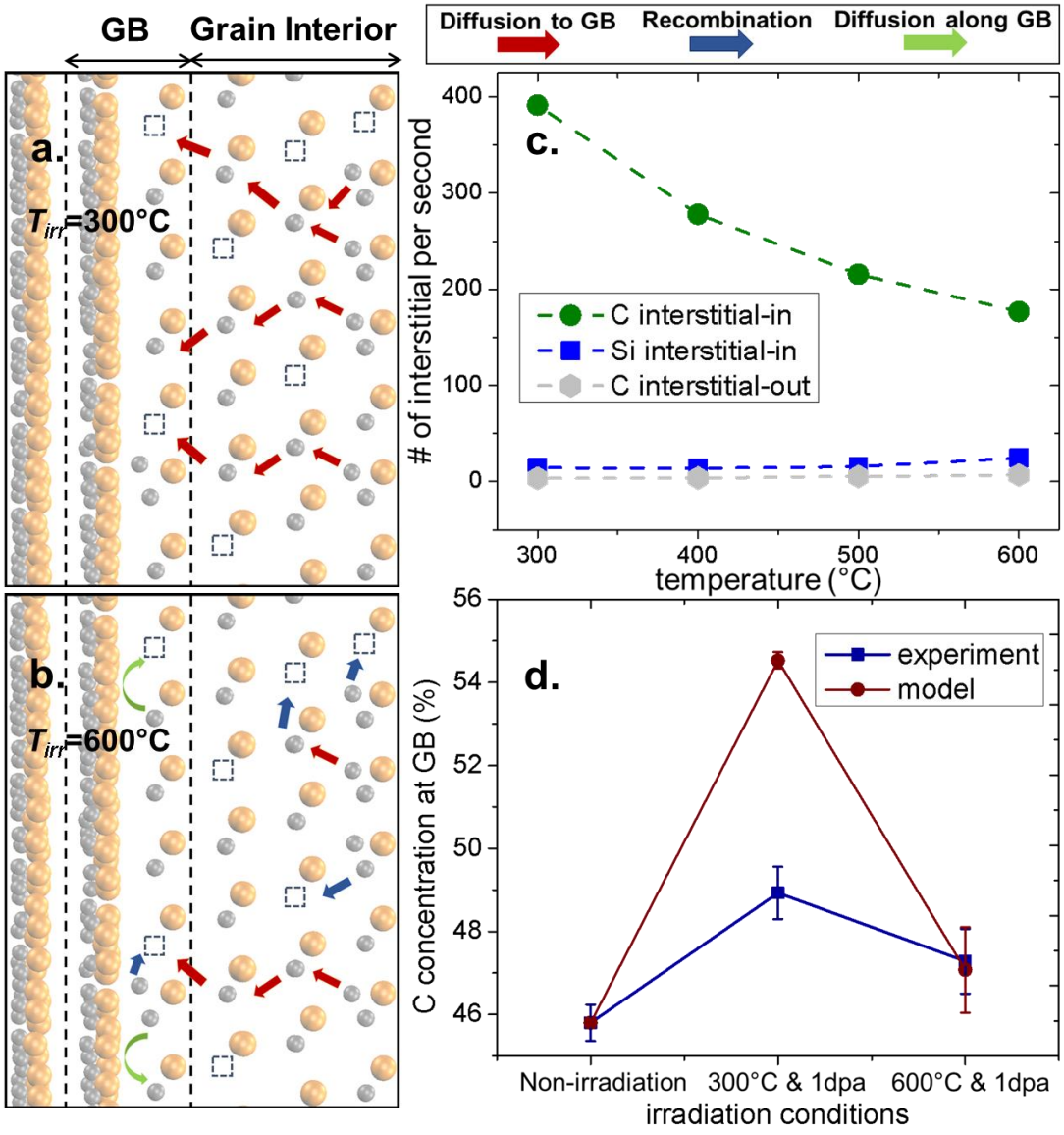

Figure 4 Schematic view of active defect kinetic processes for (a) T_{irr}=300°C and (b) T_{irr}=600°C. In these cartoons, dashed-line boxes indicate the position of the GB; orange circles represent silicon atoms and gray circles represent carbon atoms; carbon interstitials are in the dumbbell configuration; red arrows show the diffusion of carbon interstitials to GB; blue arrows show the recombination reaction of Frenkel pairs; green arrows represent diffusion of carbon interstitials along GB, which is only active at 600°C. (c) Calculated rates at which interstitials arrive at and leave the GB. (d) Comparison of carbon concentration at GBs at different irradiation conditions. Error bars for experimental concentrations are standard deviations from multiple measurements from

different GBs. Error bars for calculated concentration show calculation variations with different radiation time. More details related to the calculation are provided in Methods.

Discussion

Understanding of RIS in SiC provides the necessary foundation to explain and predict the radiation effects on multiple material properties. For example, corrosion experiments have shown that GBs in CVD-SiC are preferentially dissolved in supercritical water[3,36] and molecular dynamics (MD) simulations demonstrate that carbon enrichment at GBs suppresses GB oxidation [37]. RIS also provides an effective testbed to test our understanding of defect kinetics in ceramics, and to explore unknown mechanisms underlying defect-sink interactions. Since the final concentration profile arises from a series of synergistic defect processes that take place simultaneously both in the grain and at the defect sink, accurate predictions of RIS relies on accurate descriptions of all the defect kinetics. As we have shown in the SiC case, carbon segregation near GBs results from both the different defect diffusivities (vacancy vs. interstitial) and the different reaction energy barriers between different sublattices (silicon vs. carbon). Future studies will be needed to determine how RIS in SiC depends on the radiation conditions (e.g., radiation dose) and on GB type (e.g., is it present in CSL and low-angle GBs).

Methods

Ion irradiation and sample preparation

SiC has more than 200 polytypes and 3C-SiC is one of them which has the zinc blende crystal structure [29]. The ultra-high purity (>99.9995%) CVD 3C-SiC bulk used in our studies were sourced from two different vendors, Rohm & Haas and Insaco Inc. More specifically, thin foils prepared by mechanical polishing are using bulk SiC from Rohm & Haas and foils prepared by FIB are from Insaco Inc. As the EELS analyses show, our conclusions (i.e. the presence of intrinsic carbon depletion in pristine GBs and carbon segregation in irradiated GBs of CVD 3C-SiC), are not associated with a certain vendor or method of thin foil preparation. For the carbon ion irradiation, the bulk samples were cut into 5 mm × 5 mm × 2 mm cuboids and mirror polished on one side for the ion irradiation. One batch of the 3.15 MeV carbon ion irradiation was performed using the tandem accelerator in the Ion Beam Laboratory at the University of Wisconsin-Madison, and the other batch was performed in the Ion Beam Laboratory at the University of Michigan. The irradiation temperature was measured by thermocouples within the heated specimen stage and the temperature was controlled at the target irradiation temperature with a variance smaller than ±15°C. The fluence of the carbon ion irradiation was 1.50×10^{17} ions/cm^2. Depending on the beam flux of the accelerators, total irradiation time varied between two hours to eight hours for different samples, and the corresponding ion flux varied between 2.1×10^{13} ions/cm^2·s to 5.2×10^{12} ions/cm^2·s. According to the SRIM calculation, the damage peak for 3.15 MeV C ions in SiC is located at 2.2 μm below the surface (SI note 6). The damage level is relatively flat within the first 1 μm below the surface, which is the so-called damage plateau. All the irradiated GBs shown in Table 2 were located in the damage plateau. For non-irradiated GBs shown in Table1, some were from the irradiated bulk samples but located about 4 μm below the surface or deeper, and the other GBs were from virgin bulk 3C-SiC, so all these GBs received zero radiation damage.

To validate the discovered RIS phenomenon, we also conducted additional irradiation experiments using 4.5 MeV silicon ions on bicrystal SiC samples at 300°C. The bicrystals were fabricated by bonding two 4H-SiC single crystals together. Before the bonding, surfaces of single crystals were thoroughly cleaned to remove potential

contamination and oxide layer. Two cleaned single crystals were rotated to desired angles and pressed together at 1000°C and 30MPa for 20 hours. High quality GBs were prepared using this method. The silicon irradiation was performed in the Ion Beam Laboratory at the University of Michigan. The irradiation fluence was 1.76×10^{16} ions/cm^2 and the corresponding ion flux was 9.0×10^{11} ions/cm$^2\cdot$s, so the total irradiation time was 5.4 hours. Details of the bicsytal SiC fabrication and analyses are provided in SI note 4 and note 6.

The thin foils used for our STEM-EELS analysis were prepared either by mechanical polishing or FIB milling. For mechanical polishing, the cross-section thin foils were made by attaching two irradiated surfaces together using MBond-610 and then wedge polishing using diamond lapping films. For FIB milling, an electron backscatter diffraction (EBSD) scan was conducted first on the surface of each irradiated bulk sample. According to the location, size and crystal orientation of grains shown in the EBSD mapping, possible locations of HAGBs were identified, and 3 μm wide Pd protective layers were deposited across the HAGBs, then thin foils were prepared through the normal lift-out procedures. The EBSD and the FIB were performed using an FEI Helios PFIB G4 FIB/FESEM instrument in the Materials Science Center at the University of Wisconsin-Madison equipped with an EBSD detector. Note the thin foils prepared either by mechanical polishing or FIB were usually thicker than the desired thickness, which is about half of the inelastic scattering mean free path (IMFP) of 60 keV electrons in SiC. Additional thinning of the thin foils on both sides was performed using an FEI Fischione 1050 nanomill set at 1 kV with the angle of incident Ar ion beams set at ± 8º. Before the STEM-EELS, low magnification TEM analyses were conducted on these thin foils, which showed the grain size of the CVD 3C-SiC ranged from a few hundred nm to a few μm.

Since carbon concentrations near GBs were measured in these thin foils, it is important to confirm that these thin foils were free from hydrocarbon contamination, which might be introduced during the sample preparation or during microscopy analysis. We used the following criterion to test whether the sample was clean enough for the following EELS analyses: We focused an electron probe of the STEM on the foils in a 10 nm-wide region, and kept the probe at the same region for about 10 minutes. If there was no obvious contrast change in that region, the thin foil was regarded as clean enough. For contaminated thin

foils, the region under the electron probe would quickly become brighter in the HAADF image. We completed this test for every sample used for STEM-EELS measurement and all samples satisfied the criterion. We found a quick plasma cleaning (~ 1 min) of the thin foil using an FEI plasma cleaner was very helpful in removing possible hydrocarbon contaminations collected during the TEM analyses.

Correlative tEBSD and analysis to determine GB misorientation angles

In order to determine the misorientation angles of the analyzed GBs, correlative tEBSD and TEM analyses were performed on every thin foil prepared by FIB. The lift-out FIB foil was thinned to about 100 nm, which was thin enough for the tEBSD analysis. To improve the resolution of tEBSD mapping acquired using the FEI Helios system, optimal conditions for specimen tilt angle, working distance, accelerating voltage, beam current and step size were determined thorough a series of tests: the working distance was 4 mm, the sample tilt was 25º away from the detector, the accelerating voltage was 30 kV, the probe current was 25 nA and the step size was 10 nm. Kikuchi patterns taken at 4×4 binning were indexed using the TEAM software suite with the crystallographic information for 3C-SiC. The orientation analysis of tEBSD was performed using the TSL OIM Analysis 8 software. After the tEBSD mapping, the same thin foil was imaged using an FEI Titan to acquire bright-field (BF) TEM images. By comparing the tEBSD mapping and BF-TEM image as shown in SI note 7, the misorientation angles of all the GBs on the thin foils can be determined. Only GBs that can be tilted to the edge-on condition were selected for following EELS analyses. The selection process was completed by tiling grains along the GB to low index crystal zone axis, and taking atomic-resolution TEM image of the GB. If the GB width was narrower than 2 nm, the GB was regarded as an edge-on GB. Local thickness near the GB was measured using the spectrum imaging of zero loss EELS peak. If the GB is thicker than the desired value (~0.5 IMFP), either fine FIB milling or nano-milling should be performed in this region until the GB region is thin enough for EELS analysis.

EELS acquisition and analysis

All HAADF images and spectrum images were acquired using a Nion UltraSTEM operating at 60 kV. The convergence angle was 30 mrad and the collection angle was 48

mrad for EELS acquisition. In SI note 8, a typical core-loss EELS obtained by summing up all the signals in the narrow red box in Fig. 1b is shown. Core-loss peak of silicon (L edge, 99 eV) and carbon (K edge, 280 eV) can be easily identified. The relative carbon concentration (C_C) was measured using the following equation [38]

$$C_c = \frac{N_c}{N_c+N_{Si}} = \frac{I_C\sigma_C}{I_C\sigma_C+I_{Si}\sigma_{Si}}. \quad (4)$$

Here N_X represents the atomic density of element X in the region where EELS is collected, I_x is the integrated signal counts of the EELS core-loss peak, and σ_x is the ionization cross section of element X. The cross section for silicon and carbon were from tabulated values in Digital Micrograph software based on Hartree-Slater model. The counts integration window was 176 eV-216 eV for Si peak and 310 eV-350 eV for C peak, in order to avoid the fine structures of the EELS where the ionization cross sections were not accurate. Background subtraction was performed at 69 eV-99 eV for silicon peak and 245 eV-280 eV for carbon peak using the power law. In our analyses, the EELS signal counts for both silicon peak and carbon peak were high enough that the signal to noise ratio was over 100 (see SI note 8). For each analyzed GB, the EELS spectrum images were collected in three or more than three different locations along the GB. These locations were more than 30 nm apart from each other.

We can also exclude the possibilities that the observed carbon segregation was introduced either by possible carbon contamination during the EELS experiment or by local thickness changes near the GBs. All thin foils used for EELS analyses were baked in high temperature vacuum chambers for more than 8 hours before being inserted into the microscope. The baking process can effectively remove hydrocarbons from the sample surface. During the STEM experiment, stable ultrahigh vacuum (10^{-9} torr) at the sample was maintained and no observable contrast changes were found in the STEM-HAADF images of the regions where the electron probe was focused on, demonstrating the contamination was negligible. Near one GB, the sample thickness was quite uniform. In SI note 9, typical sample thickness profiles across a non-irradiated GB and an irradiated GB at 300ºC are shown. The standard deviation of thickness is less than 1.4%, so sample thickness variation near GB cannot explain either the intrinsic carbon depletion or the radiation-induced carbon segregation.

Rate theory model calculations

The defect concentration in the grain interior is solved based on the rate theory model discussed in previous studies [31,32]. According to the Fick's law, the defect flux to GB (*F(x,t)* in equations (2) and (3)) is equal to the defect concentration gradient near GBs times the defect diffusivities. More details about the flux is provided in SI note 10. Previous studies have shown that in SiC a large fraction of radiation-generated interstitials form defect clusters, which have much lower diffusivities than single interstitials [39–41]. Therefore, the clustering effect will substantially decrease available free interstitials that can migrate to GBs. We adapt a cluster dynamics (CD) model developed for SiC in Ref. [42] to simulate the clustering process and the details of the model are discussed in the SI note 11. According to the CD model, under our irradiation conditions only about 8% of the radiation-generated carbon interstitials are not trapped in interstitial clusters. This information is used to determine the number of available isolated interstitials when we calculate the defect flux to GBs. It is worth mentioning that in our RIS calculations we included energetics of defects in their most stable charge states. According to DFT calculations, in n-type bulk SiC, carbon vacancy, carbon interstitial, and silicon interstitial have the lowest formation energy in their neutral charge state, whereas the most stable Si vacancy has the charge state of -2 (V_{Si}^{2-}) [5,16,43]. Therefore, when calculating the defect flux from the grain interior to GBs, the migration energy barrier E_m of V_{Si}^{2-} (2.4 eV) was used, whereas for other defects we used migration energies corresponding to the neutral charge states. Note that although E_m of V_{Si}^{2-} (2.4 eV) is much lower that E_m of V_{Si}^{0} (3.4 eV) [16], the 2.4 eV E_m is still very high so vacancies in SiC are nearly immobile in the investigated temperature range (300°C to 600°C). Therefore, the migration of carbon interstitial from grain interior to GBs is the dominant driving force for carbon enrichment at GBs. For potential charge effects near GBs, a recent simulation study has found that in 3C-SiC, silicon atoms at incoherent GBs have a less positive charge than silicon in the bulk, whereas the charge state of carbon atoms at GBs is less negative than carbon in the bulk [37]. However, since the interstitials in the grain interior are most stable in their neutral charge state, we expect the charges at GBs to have a limited influence on the migration and segregation of interstitials.

The defect generation rate (G) at GBs is calculated using the following equation

$$G = \Gamma \eta \alpha_n \rho. \quad (5)$$

Here Γ is the dose rate, which is 1 dpa divided by total irradiation time; η is the intracascade recombination rate, which is set as 0.5 based on a previous molecular dynamics (MD) study [44]; a_n is the generation fraction of defect of type n, which is taken from MD simulations reported in Ref. [45]; ρ is the atomic density of SiC, which is equal to 9.64×10^{26} atoms/m^3. The reaction coefficient of vacancy-interstitial recombination (R) is defined as [46]

$$R = 4\pi r_c (D_i + D_v). \quad (6)$$

Here, r_c is the recombination reaction radius and D_i and D_v are the diffusivities of interstitial and vacancy, respectively. The general equation for diffusivity is

$$D = D_0 \exp\left(-\frac{E_m}{k_B T}\right), \quad (7)$$

where k_B is the Boltzmann constant and T is the temperature. The prefactor D_0, migration barrier E_m, as well as α_n and r_c for all four kinds of point defects are summarized in Table 3. As discussed in the main text, D_i for carbon is an important parameter in the rate theory model. Self-diffusivities of carbon along GBs and in grain interiors have been determined based on experiments in a previous study, where ^{14}C isotope was traced in CVD-SiC [47]. The same study also reported the diffusion activation energy E_{act}, which was determined by fitting the measured diffusivity to the Arrhenius equation. E_{act} is equal to the sum of the formation energy E_f and the migration energy E_m of carbon interstitials. Taking the values from Ref.[47], we can write

$$E_{act}^{GB} = E_f^{GB} + E_m^{GB} = 5.84 \text{ eV}, \quad (8)$$

$$E_{act}^{bulk} = E_f^{bulk} + E_m^{bulk} = 8.72 \text{ eV}. \quad (9)$$

Formation energies of carbon interstitials at the GB (E_f^{GB}) and in the grain interior (E_f^{bulk}) depend on the carbon chemical potentials in SiC, which are difficult to quantify for the study in Ref. [47]. Therefore, to estimate the carbon interstitial migration barrier along the GB (E_m^{GB}), we subtract equation (8) from equation (9), so that the chemical potential for carbon cancels out

$$E_m^{GB} = (E_{act}^{GB} - E_{act}^{bulk}) - (E_f^{GB} - E_f^{bulk}) + E_m^{Bulk}. \quad (10)$$

The difference in activation energies (-2.88 eV) between the GB and the bulk is taken from the trace diffusion experiment [47]. Previous density functional theory (DFT) calculations have found the migration barrier for C interstitial in the bulk is 0.67 eV [16]. Therefore, as long as the difference in formation energies at the GB and in the bulk is known, the migration barrier of carbon interstitial along the GB can be estimated. We have applied DFT to calculate this difference. More specifically, a supercell containing one tilt GB and 552 atoms is used to calculate E_f of carbon interstitials at GB and a supercell containing 216 atoms to calculate E_f in the bulk. According to these calculations, the difference in E_f of carbon interstitial on the GB and in the bulk is -3.97 eV. By plugging in all these values into equation (10), we get the migration barrier for carbon interstitial at GB, which is equal to 1.76 eV. The details of DFT calculations of formation energies are discussed in SI note 12. We have also performed separate MD simulations of carbon interstitial diffusion along a series of tilt GBs in SiC [33], which shows the migration barrier for carbon to diffuse along the tilt axis should be larger than 1.6 eV. Therefore, the estimated migration barrier based on the isotope diffusion experiment falls in the range of values determined directly from the MD simulations. After the defect concentrations at the GB are calculated, the corresponding relative carbon concentration ($C_{C,cal}$) can be calculated using the following equation

$$C_{C,cal} = \frac{C_{C,i} - C_{C,v} + 45.8\ at.\%}{C_{C,i} - C_{C,v} + C_{Si,i} - C_{Si,v} + 1}. \quad (11)$$

Here $C_{X,i/v}$ is the atomic ratio of interstitial/vacancy of element X at the GBs after the irradiation, and 45.8 at. % is the relative carbon concentration in pristine GBs, as determined by our EELS analysis.

Table 3 Parameter used in the rate theory calculations in equation (2) and (3). "I" stands for interstitial and "V" stands for vacancy. D_0, a_n, r_c and E_m (except for carbon interstitial) are from the previous study [31].

	D_0 / m^2/s	E_m /eV	a_n	r_c/nm
Si, I	3.30×10^{-7}	0.83	0.07	0.63
Si, V	7.26×10^{-8}	2.40		
C, I	1.23×10^{-7}	1.76	0.43	0.21
C, V	7.26×10^{-8}	3.66		

In Fig. 4c, the rate of interstitials arriving at GB is equal to the interstitial flux to GB multiplied by the GB surface area, which is 1 μm^2 (i.e., the product of the GB side lengths assumed as 1 μm). The rate of carbon interstitials leaving GB is equal to the carbon interstitial flux along GBs multiplied by the interface area between GB and other sinks (e.g., surfaces and triple junctions). The interface area is assumed as the product of the GB half width (~1 nm) and GB side length (~1 μm), so the total interface area on both ends of the GB is 2×10^{-3} μm^2. The interstitial fluxes in the middle of the irradiation experiment are used for calculating the arrive and leave rates of interstitials shown in Fig. 4c.

The rate theory equations (2) and (3) are solved in the space domain $0 \leq x \leq l$, where l is the length of the GB and is assumed to be equal to 1 μm based on our TEM analysis. Since the total irradiation time in our experiment varies between 2 to 8 hours, the rate theory equations are also solved in the time domain $0 \leq t \leq T$, where T is set between 2 to 8 hours. Different total irradiation time changes the defect flux to GBs, defect

generation rates and other defect kinetic processes, so the calculated GB carbon concentrations will be different. The average of the GB carbon compositions calculated with different total irradiation time is plotted in Fig. 4d, and the range of the calculated composition values is taken as the uncertainty of the calculations.

References

1. Van Swygenhoven, H. Grain Boundaries and Dislocations. *Science* **296**, 66–67 (2002).
2. Shen, Z., Wagoner, R. H. & Clark, W. A. T. Dislocation and grain boundary interactions in metals. *Acta Metall.* **36**, 3231–3242 (1988).
3. Allen, T., Lance, M., Meyer, H. & Walker, L. Corrosion of CVD Silicon Carbide in 500 C Supercritical Water. *J. Am. Ceram. Soc.* **90**, 315–318 (2007).
4. Gleiter, H. Grain boundaries as point defect sources or sinks-diffusional creep. *Acta Metall.* **27**, 187–192 (1979).
5. Shrader, D. *et al.* Ag diffusion in cubic silicon carbide. *J. Nucl. Mater.* **408**, 257–271 (2011).
6. Jiao, Z. & Was, G. S. Novel features of radiation-induced segregation and radiation-induced precipitation in austenitic stainless steels. *Acta Mater.* **59**, 1220–1238 (2011).
7. Etienne, A., Radiguet, B., Cunningham, N. J., Odette, G. R. & Pareige, P. Atomic scale investigation of radiation-induced segregation in austenitic stainless steels. *J. Nucl. Mater.* **406**, 244–250 (2010).
8. Field, K. G. *et al.* Dependence on grain boundary structure of radiation induced segregation in a 9 wt.% Cr model ferritic/martensitic steel. *J. Nucl. Mater.* **435**, 172–180 (2013).
9. Rehn, L. E., Okamoto, P. R. & Wiedersich, H. Dose dependence of radiation-induced segregation in Ni-1 at% Si. *J. Nucl. Mater.* **80**, 172–179 (1979).
10. Was, G. S. *et al.* Assessment of radiation-induced segregation mechanisms in austenitic and ferritic-martensitic alloys. *J. Nucl. Mater.* **411**, 41–50 (2011).
11. Busby, J. ., Was, G. . & Kenik, E. . Isolating the effect of radiation-induced segregation in irradiation-assisted stress corrosion cracking of austenitic stainless steels. *J. Nucl. Mater.* **302**, 20–40 (2002).
12. Bruemmer, S. M. & Was, G. S. Microstructural and microchemical mechanisms controlling intergranular stress corrosion cracking in light-water-reactor systems. *J. Nucl. Mater.* **216**, 348–363 (1994).
13. Olesinski, R. W. & Abbaschian, G. J. The C−Si (Carbon-Silicon) system. *Bull. Alloy Phase Diagrams* **5**, 486–489 (1984).
14. Katoh, Y., Snead, L. L., Szlufarska, I. & Weber, W. J. Radiation effects in SiC for nuclear structural applications. *Curr. Opin. Solid State Mater. Sci.* **16**, 143–152 (2012).
15. Mehregany, M. & Zorman, C. A. SiC MEMS: opportunities and challenges for applications in harsh environments. *Thin Solid Films* **355**, 518–524 (1999).

16. Zheng, M. J., Swaminathan, N., Morgan, D. & Szlufarska, I. Energy barriers for point-defect reactions in 3C-SiC. *Phys. Rev. B* **88**, 1–15 (2013).
17. Krivanek, O. L. *et al.* An electron microscope for the aberration-corrected era. *Ultramicroscopy* **108**, 179–195 (2008).
18. Tan, L., Allen, T. R., Hunn, J. D. & Miller, J. H. EBSD for microstructure and property characterization of the SiC-coating in TRISO fuel particles. *J. Nucl. Mater.* **372**, 400–404 (2008).
19. Katoh, Y. *et al.* Current status and critical issues for development of SiC composites for fusion applications. *J. Nucl. Mater.* **367-370 A**, 659–671 (2007).
20. Fu, X.-A., Dunning, J. L., Zorman, C. A. & Mehregany, M. Polycrystalline 3C-SiC thin films deposited by dual precursor LPCVD for MEMS applications. *Sensors Actuators A Phys.* **119**, 169–176 (2005).
21. Kondo, S., Katoh, Y. & Snead, L. L. Analysis of grain boundary sinks and interstitial diffusion in neutron-irradiated SiC. *Phys. Rev. B* **83**, 1–6 (2011).
22. Wang, X. *et al.* Evidence for cascade overlap and grain boundary enhanced amorphization in silicon carbide irradiated with Kr ions. *Acta Mater.* **99**, 7–15 (2015).
23. Jiang, H. & Szlufarska, I. Small-Angle Twist Grain Boundaries as Sinks for Point Defects. *Sci. Rep.* **8**, 3736–3749 (2018).
24. Gao, F., Chen, D., Hu, W. & Weber, W. J. Energy dissipation and defect generation in nanocrystalline silicon carbide. *Phys. Rev. B* **81**, 1–8 (2010).
25. Ziegler, J. F., Ziegler, M. D. & Biersack, J. P. SRIM – The stopping and range of ions in matter (2010). *Nucl. Instruments Methods Phys. Res. Sect. B Beam Interact. with Mater. Atoms* **268**, 1818–1823 (2010).
26. Stoller, R. E. *et al.* On the use of SRIM for computing radiation damage exposure. *Nucl. Instruments Methods Phys. Res. Sect. B Beam Interact. with Mater. Atoms* **310**, 75–80 (2013).
27. Jiang, C., Zheng, M. J., Morgan, D. & Szlufarska, I. Amorphization driven by defect-induced mechanical instability. *Phys. Rev. Lett.* **111**, 1–5 (2013).
28. Lucas, G. & Pizzagalli, L. Ab initio molecular dynamics calculations of threshold displacement energies in silicon carbide. *Phys. Rev. B* **72**, 161202(R) (2005).
29. Snead, L. L. *et al.* Handbook of SiC properties for fuel performance modeling. *J. Nucl. Mater.* **371**, 329–377 (2007).
30. Ardell, A. J. & Bellon, P. Radiation-induced solute segregation in metallic alloys. *Curr. Opin. Solid State Mater. Sci.* **20**, 115–139 (2016).
31. Swaminathan, N., Morgan, D. & Szlufarska, I. Role of recombination kinetics and grain size in radiation-induced amorphization. *Phys. Rev. B* **86**, 1–16 (2012).
32. Swaminathan, N., Morgan, D. & Szlufarska, I. Ab initio based rate theory model of radiation induced amorphization in beta-SiC. *J. Nucl. Mater.* **414**, 431–439 (2011).
33. Jiang, H., Wang, X. & Szlufarska, I. The multiple roles of small-angle tilt grain boundaries in annihilating radiation damage in SiC. *Sci. Rep.* **7**, 42358 (2017).
34. Zhang, Y. *et al.* Ionization-induced annealing of pre-existing defects in silicon carbide. *Nat. Commun.* **6**, 8049 (2015).
35. Hua, W. *et al.* Ion-irradiation-induced athermal annealing of helium bubbles in SiC. *Nucl. Instruments Methods Phys. Res. Sect. B Beam Interact. with Mater.*

Atoms **268**, 2325–2328 (2010).
36. Park, J. Y. *et al.* Long-term corrosion behavior of CVD SiC in 360 C water and 400 C steam. *J. Nucl. Mater.* **443**, 603–607 (2013).
37. Liu, C., Xi, J. & Szlufarska, I. Sensitivity of SiC Grain Boundaries to Oxidation. *J. Phys. Chem. C* **123**, 11546–11554 (2019).
38. Egerton, R. *Electron Energy-Loss Spectroscopy in the Electron Microscope*. (Springer, 2011).
39. Jiang, C., Morgan, D. & Szlufarska, I. Structures and stabilities of small carbon interstitial clusters in cubic silicon carbide. *Acta Mater.* **62**, 162–172 (2014).
40. Katoh, Y., Hashimoto, N., Kondo, S., Snead, L. L. & Kohyama, A. Microstructural development in cubic silicon carbide during irradiation at elevated temperatures. *J. Nucl. Mater.* **351**, 228–240 (2006).
41. Jiang, H., He, L., Morgan, D., Voyles, P. M. & Szlufarska, I. Radiation-induced mobility of small defect clusters in covalent materials. *Phys. Rev. B* **94**, (2016).
42. Liu, C. *et al.* Evolution of small defect clusters in ion-irradiated 3C-SiC: Combined cluster dynamics modeling and experimental study. *Acta Mater.* **125**, 377–389 (2017).
43. Bockstedte, M., Mattausch, A. & Pankratov, O. Ab initio study of the migration of intrinsic defects in 3C-SiC. *Phys. Rev. B* 205201 (2003) doi:10.1103/PhysRevB.68.205201.
44. Devanathan, R., Weber, W. J. & Gao, F. Atomic scale simulation of defect production in irradiated 3C-SiC. *J. Appl. Phys.* **90**, 2303–2309 (2001).
45. Swaminathan, N., Kamenski, P. J., Morgan, D. & Szlufarska, I. Effects of grain size and grain boundaries on defect production in nanocrystalline 3C-SiC. *Acta Mater.* **58**, 2843–2853 (2010).
46. Waite, T. R. General theory of bimolecular reaction rates in solids and liquids. *J. Chem. Phys.* **28**, 103–106 (1958).
47. Hon, M. H. & Davis, R. F. Self-diffusion of 14C in polycrystalline beta-SiC. *J. Mater. Sci.* **14**, 2411–2421 (1979).

Data Availability

The authors declare that all data supporting the findings of this study are available within the paper and its supplementary information files.

to these results of federally sponsored research in accordance with the DOE Public Access Plan (http://energy.gov/downloads/doe-public-access-plan).

Code Availability

The code used for calculating carbon concentrations at grain boundaries is provided in the Supplementary Information.

Acknowledgments

The authors acknowledge the US Department of Energy Basic Energy Sciences for funding this research (Fund number DE-FG02-08ER46493). The authors also gratefully acknowledge use of facilities and instrumentation supported by NSF through the University of Wisconsin Materials Research Science and Engineering Center (DMR-1720415). The electron microscopy research was conducted as part of a user project through Oak Ridge National Laboratory's Center for Nanophase Materials Sciences (CNMS), which is a U.S. Department of Energy Office of Science User Facility.